J Nanopart Res (2018) 20: 159
https://doi.org/10.1007/s11051-018-4261-z

RESEARCH PAPER

The synergistic effect of phase heterojunction and surface heterojunction to improve photocatalytic activity of $V_O^{\bullet}$–TiO_2: the co-catalytic effect of $H_3PW_{12}O_{40}$

Haiyan Li · Shengnan Cai · Pengfei Yang · Yan Bai · Dongbin Dang

Received: 8 January 2018 / Accepted: 24 May 2018 / Published online: 9 June 2018

Abstract With nanotube titanic acid (abbreviated as NTA) and the 12-tungstophosphoric acid ($H_3PW_{12}O_{40}$•xH_2O, denoted as HPW) as start materials, respectively, according to a simple hydrothermal process in acid medium, we successfully prepared HPW modified $V_O^{\bullet}$–TiO_2 composite photocatalysts. During heat treatment companied by the transformation of NTA to TiO_2, a kind of single-electron-trapped oxygen vacancy ($V_O^{\bullet}$) could be formed contributing to the visible light absorption of catalysts. The morphology, phase and chemical structure, optical and electronic properties, and so on of the produced catalysts with various HPW loadings are characterized. The size range of synthesized photocatalyst nanoparticles are about 10~50 nm. Taking aqueous rhodamine B (RhB) dye as model pollutant, we carried out photocatalytic activity test of the achieved catalysts, revealing that the hybrid photocatalysts display significantly enhanced visible light-driven ($\lambda \geq 420$ nm) photocatalytic activity for degradation of RhB. Among various catalysts, HPWN-0.1-120 composite with nominal loading of 0.1 g HPW and heat treatment temperature of 120 °C possesses the highest photocatalytic performance in visible light, which is closely related to the co-effect of phase heterojunction of rutile/anatase, surface heterojunction of anatase/HPW, and oxygen vacancy ($V_O^{\bullet}$). The two types of heterojunction promote greatly the separation efficiency of photoelectrons and photoholes and oxygen vacancy lures response of catalysts to visible light.

Keywords Tungstophosphoric acid · Oxygen vacancy · Heterojunction · Photocatalytic pollutant elimination · Titanium dioxide · Nanostructured catalysts

H. Li (✉) · S. Cai · P. Yang · Y. Bai (✉) · D. Dang
Henan Key Laboratory of Polyoxometalate Chemistry, College of Chemistry and Chemical Engineering, Henan University, Kaifeng 475004, China
e-mail: lihaiyan@henu.edu.cn
e-mail: baiyan@henu.edu.cn

Introduction

Since a new era on photocatalysis was ushered in 1972 (Fujishima and Honda 1972), semiconductor-based photocatalysis has attracted wide interests because of its ability to directly utilize solar energy to perform multitudinous catalytic reactions such as water splitting to produce H_2 (Reza Gholipour et al. 2015; Willkomm et al. 2016), reduction of CO_2 to hydrocarbon fuels (White et al. 2015; Zhang et al. 2015; Yu et al. 2014; Low et al. 2017; Xu et al. 2015), degradation of organic pollutants (Dong et al. 2015; Wang et al. 2016), bacteria disinfection (Ruales-Lonfat et al. 2015), and selective synthesis of organic compounds (Prier et al. 2013). Upsettingly, the applications of photocatalysis in the practical process are still limited owing to low photocatalytic efficiency (Li et al. 2016). A main influence factor is just the fast electron–hole recombination playing a negative role in the photocatalytic processes (Qu and Duan 2013). To inhibit effectively the recombination of the electron–hole pairs and thereby improving the enhanced photocatalytic activity, various strategies have been employed such as doping with metal (Choi et al. 1994) or nonmetal

(Asahi et al. 2001), noble-metal loading (Zhu et al. 2012) and the design of heterojunction photocatalysts (Zhang et al. 2013; Hong et al. 2016), and so on. Among them, the type-II heterojunction photocatalysts, composed of the two different semiconductors or two different phases of a semiconductor, have been payed more attention due to exhibiting good electron–hole separation efficiency, wide light absorption range, and fast mass transfer (Yu et al. 2001; Yu et al. 2005; Li and Gray 2007; Chen et al. 2015). For example, in 2001, an anatase–brookite dual-phase type-II heterojunction photocatalyst was prepared by hydrolyzing titanium tetraisopropoxide in H_2O or 1:1 ethanol–H_2O solution. The prepared catalysts showed greatly enhanced photocatalytic activity higher than that of one consisting of pure anatase due to the formation of heterojunction between the brookite and the anatase inducing a higher separation efficiency of the electron–hole pairs and thereby promoting the photocatalytic activity (Yu et al. 2001).

Since nanotube titanic acid was reported (Kasuga et al. 1998; Yin et al. 1999), it has been payed enormous attention in photocatalysis field due to its large surface area, mesoporous feature, and fast carrier migration rate via tubular structure. A systematic research about nanotube titanic acid ($H_2Ti_2O_4(OH)_2$, abbreviated as NTA) revealed that, after it undergoes heat-treating, a novel anatase TiO_2 modified by a mass of intrinsic defects: single-electron-trapped oxygen vacancy (SETOV, $V_O^{\bullet}$) could be achieved. The TiO_2 exhibits photo-absorption to visible light with corresponding absorption band edge of ~ 450 nm (Yang et al. 2003; Zhang et al. 2004a, b; Wang et al. 2010; Wang et al. 2011), which derived from an intermediate energy level formed by $V_O^{\bullet}$, located at 0.90–1.20 eV below the conduction band (CB) of TiO_2 according to theoretical calculation results (Li et al. 2015). This is infusive, and however, a pity is left that no visible light-driven photoactivity is detected, which is owing to the $V_O^{\bullet}$ generated via the intralayered dehydration of NTA (Zhang et al. 2004a), hinting that it exists mainly in the bulk of TiO_2 and is very stable. In the absence of the efficient electron capture centers, though the sub-band formed by $V_O^{\bullet}$ induces visible light absorption, simultaneously, it also becomes e^-–h^+ recombination center corresponding to theoretical calculation results (Li et al. 2015). This is detrimental to the enhancement of the photocatalytic activity. Therefore, it is expected to explore the efficient electron capture to improve the photoactivity of $V_O^{\bullet}$–TiO_2.

More recently, polyoxometalates (abbreviated as POMs) were reported as efficient electron acceptors by many researches (Li et al. 2010a, b; Xu et al. 2010; Lu et al. 2012; Zhang et al. 2012). POMs are a kind of polyanionic clusters composed of transition metals (primarily V, W, Nb, Mo, or Ta) and oxygen. The preparation of them is relatively simple and straightforward, usually obtained via hydrothermal method in one pot (Karkas et al. 2014). Among the various POMs, $H_3PW_{12}O_{40}$ (12-tungstophosphoric acid) with well-defined Keggin structure, possessing similar photochemical characteristics with semiconductor photocatalysts, has widely been used in heterogeneous photocatalysis field owing to efficient electron reception and transfer ability from $H_3PW_{12}O_{40}$ to oxygen species present in the reaction system. A series of different content $H_3PW_{12}O_{40}$ loaded mesoporous $H_3PW_{12}O_{40}$/TiO_2 composite materials were fabricated by an evaporation-induced self-assembly technology and compared to neat TiO_2, the composite photocatalyst exhibited enhanced photocatalytic activity for the degradation of methyl orange under solar simulating Xe lamp irradiation (Li et al. 2010a). The porous $H_3PW_{12}O_{40}$/TiO_2 nanocomposites were also prepared via sol–gel chemistry combined with solvothermal treatment and the obtained compounds displayed higher photocatalytic activity towards the degradation of aqueous phthalate esters pollutant under the simulated sunlight irradiation ($\lambda = 320$–680 nm), which is closely related to the synergistic effect between the Keggin unit and TiO_2 network (Xu et al. 2010).

For the purpose of decreasing the recombination rate of the photogenerated carriers in the oxygen vacancy modified-TiO_2 ($V_O^{\bullet}$–TiO_2) to facilitate its photocatalytic efficiency, in the present study, we introduced $H_3PW_{12}O_{40}$ (denoted as HPW) with Keggin unit onto $V_O^{\bullet}$–TiO_2 using NTA as starting material by a simple hydrothermal synthesis. The photocatalytic efficiency of as-fabricated HPW modified $V_O^{\bullet}$–TiO_2 hybrids was evaluated by monitoring the degradation of rhodamine B (RhB) dye with visible irradiation ($\lambda \geq 420$ nm). RhB was completely decomposed after only irradiation of 40 min upon 0.1 g of HPW loaded on the surface of $V_O^{\bullet}$–TiO_2 (the sample HPWN-0.1-120), which is ascribed to the co-effect of phase heterojunction of rutile/anatase, surface heterojunction of anatase/HPW, and oxygen vacancy ($V_O^{\bullet}$). The two-type heterojunction promoted greatly the separation efficiency of photoelectrons and photoholes and oxygen vacancy ($V_O^{\bullet}$) lured

response of catalysts to visible light. Aforementioned, although there are many papers that reported the modification of TiO_2 with HPW, most of which is only photoactivity under UV irradiation. The prepared HPW/$V_O^{\bullet}$–TiO_2 by us in the work can be motivated by visible light due to the existence of the sub-band derived from $V_O^{\bullet}$ in the forbidden band of TiO_2.

Experimental

Preparation of nanotube titanic acid (abbreviated as NTA)

Taking commercial P25 TiO_2 and certain concentrations of NaOH aqueous solution (10 mol/L) as the raw materials, we synthesized nanotube titanic acid in a hydrothermal process. The detailed process of NTA preparation can be vided literature (Li et al. 2015).

Preparation of HPW/$V_O^{\bullet}$–TiO_2 hybrid photocatalysts

A series of HPW-loaded $V_O^{\bullet}$–TiO_2 composites were synthesized by a simple hydrothermal process, typically, 1 g NTA as the base, and the desired amount of homemade HPW (0.05, 0.1, 0.3, 0.5, and 0.7 g) was dissolved into HCl solution (2 mol/L, 15 mL) to stir for 1 h, and the obtained HPW/HCl solution was denoted as A; 1 g NTA was dispersed into deionized water (15 mL) under vigorous stirring for 1 h to achieve good dispersion of NTA and the resulting NTA turbid liquid was denoted as B. Following, the solution A was added dropwise into turbid liquid B under continuous stirring, and the obtained mixture kept to be stirred for 1 h at room temperature to achieve adsorption equilibrium and uniform mixing between HPW and NTA. Then, it was transferred into a 100-mL Teflon-lined autoclave to undergo hydrothermal reaction for 24 h at 150°C. After cooling to room temperature, the resulting product was washed with deionized water about three times until Cl^- cannot be detected and collected by centrifugation. After that, the sample was dried in vacuum oven at 60 °C. To research the influence of thermodynamic condition on the photocatalytic performance of the obtained catalysts, a series of composite catalysts with 0.1 g HPW loading were prepared under the different hydrothermal temperature. The prepared catalysts were denoted as HPWN-*x*-T, where *x* represents the loading content of HPW and T refers to hydrothermal temperature. Meanwhile, the effect of the concentration of HCl solution used as solvent to dissolve HPW on the photoactivity was also referred to.

Structural characterization of catalysts

The crystal structures of catalysts were recorded by X-ray diffraction (XRD) patterns on a X'Pert Philips diffractometer equipped with Cu Kα irradiation. The UV–vis absorption spectrum of catalysts was obtained by a Shimadzu UV-2600 UV/Vis spectrometer with $BaSO_4$ as a reflectance standard over a range of 200–800 nm. X-ray photoelectron spectroscopy (XPS) measurement was carried out on ESCALAB 250Xi X-ray photoelectron spectrometer (Al Kα, $h\nu$ = 1486.6 eV) and the spectra were calibrated using C 1s peak as a standard at 284.8 eV. The morphologies of catalysts were determined using JEM-2100 transmission electron microscope (TEM). The electron spin resonance (ESR) spectra of photocatalysts were conducted to prove the presence of $V_O^{\bullet}$ with Brüker ESP 300E apparatus at room temperature and in ambient air. Gilden FluoroSENSfluorescence spectrometer was used to carry out photoluminescence (PL) measurements of catalysts. With the help of energy dispersive X-ray spectrometer (EDX) equipped on field emission scanning electron microscopy (FESEM, JEOL JSM-7610F), the elemental mappings of catalyst were gained.

Photocatalytic activity test of catalysts

Taking the visible light-driven degradation of rhodamine B (RhB) as the probe reaction, the photocatalytic activity of the obtained HPW/$V_O^{\bullet}$–TiO_2 nanocomposites was studied. The visible light was obtained from a 300 W Xe lamp equipped with a cutoff filter ($\lambda \geq 420$ nm). Firstly, 0.1 g photocatalyst powder was dispersed in 100 mL solution of RhB (20 mg/L). To achieve adsorption–desorption equilibrium between the photocatalyst and reaction substrate, before irradiation, the suspension composed of photocatalyst powder and RhB was magnetically stirred in dark for 2 h. The photodegradation efficiency of RhB was monitored by detecting the change of absorbance of RhB in the residual solution at 554 nm using the UV–vis spectrophotometer. In the time interval of 10 min, a 4-mL aliquot suspension was taken out and centrifuged to remove photocatalyst

powder. The degradation percentage of RhB was calculated by the formula: $(1 - C_t / C_0) \times 100\%$, where C_0 represents the initial concentration of RhB and C_t refers to the concentration at the different moment.

Photoelectrochemical tests

With the help of a three-electrode system on electrochemical workstation (CHI600e, Shanghai Chenhua, China), photoelectrochemical properties of catalysts are tested. The Na_2SO_3 aqueous solution (1 mol/L) is used as electrolyte. The as-synthesized photocatalyst spread on FTO substrate (1 cm × 1.5 cm) acted as working electrode, a platinum wire as counter electrode, and a standard Ag/AgCl electrode as reference electrode in the whole photoelectrochemical measurement process.

Results and discussion

The XRD patterns of the fabricated various photocatalysts were shown in Fig. 1. The crystalline phase of the obtained samples is highly dependent on the solvent and hydrothermal temperature used during catalysts preparation. As described in Fig. 1a, when the hydrothermal temperature was 150 °C and the used solvent was acidic due to the addition of HCl, all the composite photocatalysts with the different HPW loadings mainly show well-indexed anatase phase (JCPDS No. 21-1272), except for a small amount of brookite (the diffraction peak of the brookite is around $2\theta = 30.8°$ corresponding to (121) face, JCPDS No. 29-1360), which corresponds to the reports in the previous literatures (Li and Gray 2007; Lei and Duan 2008; Murakami et al. 2010; Yu et al. 2005, 2001, 2003). Upon HPW loaded onto the surface of $V_O^{\bullet}$–TiO_2, no the diffraction peaks corresponding to the HPW Keggin unit are observed for all the as-prepared HPW/$V_O^{\bullet}$–TiO_2 composite catalysts due to the less content or the high dispersion of amorphous HPW (Mattos de et al. 2017; Heng et al. 2017; Zhang et al. 2008). Moreover, it should be noted that the characteristic peak of anatase TiO_2 at $2\theta = 25°$ gradually weaken as increasing HPW content, suggesting that the more HPW loading may suppress the grain growth of TiO_2. Interestingly, when the reaction temperature is 120°C, the obtained catalyst HPWN-0.1-120 exhibits mixed crystal structure of anatase and rutile (Fig. 1b) without brookite, which can be clearly observed from the enlarged XRD patterns from $2\theta = 20$ to 33° shown in inset in Fig. 1b. In consideration of the addition of HCl in the hydrothermal process, the presence of the mixed phase of anatase and rutile seems also reasonable (Li and Gray 2007; Lei and Duan 2008). With the increasing heat-treated temperature of 180 and 200 °C, neither the rutile phase nor the brookite phase was detected except for only the anatase phase pattern. The change trend seems to be inconsistent with that reported in the literature in which the relative fraction of rutile phase in the crystal structures of TiO_2 increases gradually with the increasing hydrothermal temperature in HCl medium (Murakami et al. 2010). This difference may be related to the different precursor used in the study. In a word, the presence of the mixed phase would be favorable to the enhanced photocatalytic activity.

As one of POMs, phosphotungstic acid with strong acidity can also affect the crystal phase transition of TiO_2. From a comparative result on XRD shown in Fig 1c, at 120 °C without HPW loading, the pure anatase TiO_2 is observed in the water media, and on the contrary, the bare rutile TiO_2 is obtained in acidic medium. After loading HPW onto the surface of $V_O^{\bullet}$–TiO_2, it can be clearly seen that only a small amount of rutile phase TiO_2 can be detected though in the same acid medium, implying that HPW may suppress the formation of the rutile. Moreover, the effect of the concentrations of hydrochloric acid on crystal structure is further researched. In Fig. 1d, the obvious diffraction peak corresponding to rutile phase cannot be detected until the concentration of HCl reaches 2 mol/L. The fraction of rutile phase in the synthesized composites increases gradually as the concentration of HCl greater than 2 mol/L, and conversely, the fraction of anatase phase decreases gradually, which is consistent with the observations reported in the literature (Li and Gray 2007; Wu et al. 2002).

For the sake of proving the presence and examining the structural stability of HPW in the obtained composite materials, IR spectra measurements of the parent HPW and a series of HPW/$V_O^{\bullet}$–TiO_2 composites with the different HPW loadings have been carried out. In Fig. 2, for the parent HPW, there are four obvious characteristic frequencies corresponding to the Keggin unit at 1079, 983, 893, and 796 cm^{-1}, which are assigned to the vibrations of the P–O bonds of the PO_4 units, W=O bonds, and two W–O–W bonds of the

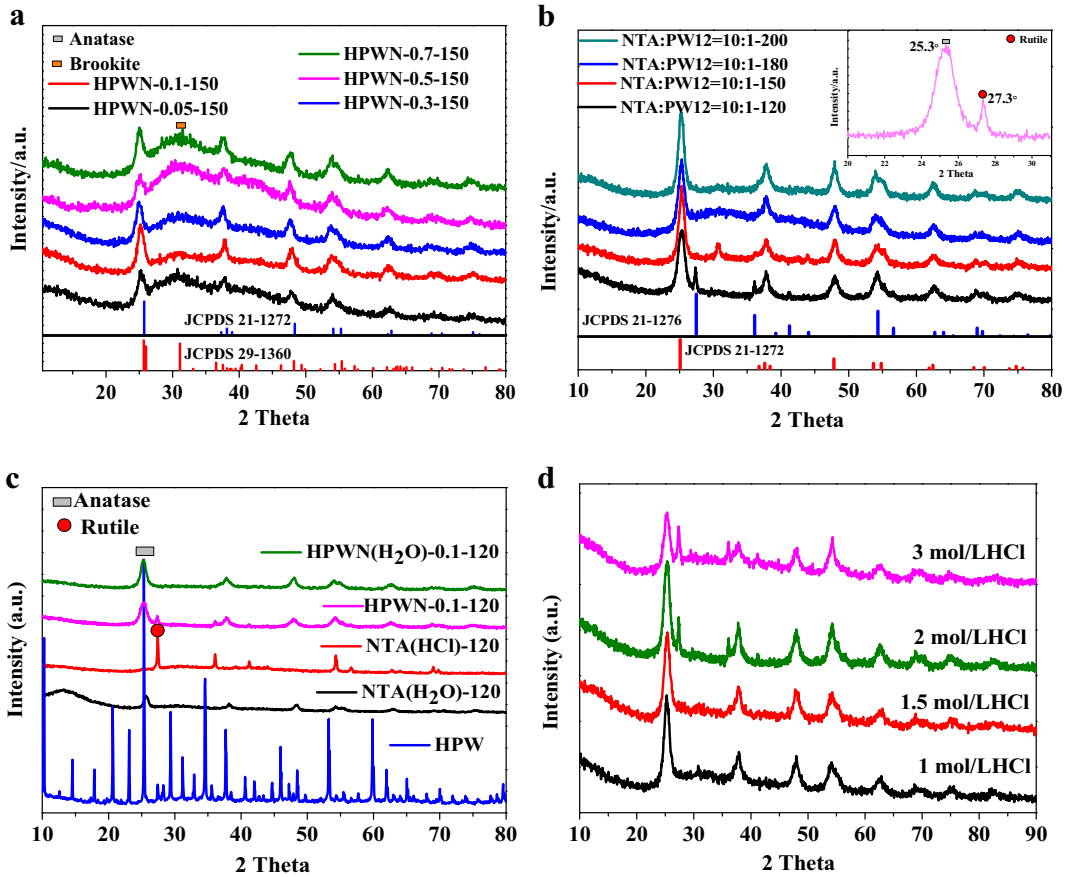

Fig. 1 XRD patterns of **a** HPWN-*x*-150 ($x = 0.05$, 0.1, 0.3, 0.5, 0.7); **b** HPWN-0.1-T ($T = 120$, 150, 180, 200); **c** HPW, NTA(H_2O)-120, NTA(HCl)-120, HPWN(H_2O)-0.1-120, and HPWN-0.1-120; and **d** HPWN-0.1-120 in the different concentrations of hydrochloric acid solution (1, 1.5, 2, 3 mol/L). The inset in **b** is the magnified XRD patterns from $2\theta = 20$ to 33° for the sample HPWN-0.1-120

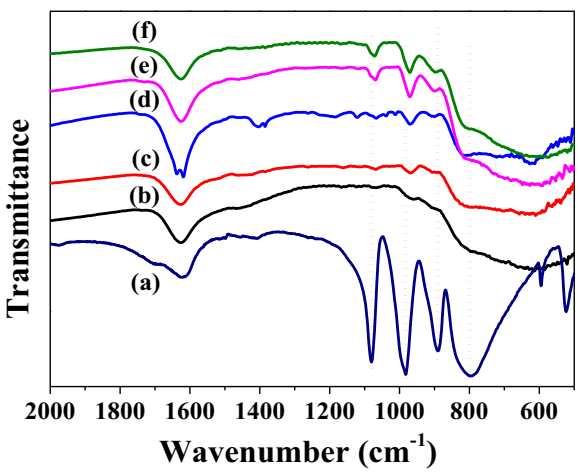

Fig. 2 IR spectra of (a) the parent HPW and HPW/$V_O^{\bullet}$-TiO_2 composites with the different HPW loadings (b) 0.05, (c) 0.1, (d) 0.3, (e) 0.5, and (f) 0.7

Keggin unit, respectively (Li et al. 2010b; Sun et al. 2015). For the fabricated composite materials, the aforementioned characteristic peaks corresponding to the Keggin unit of HPW can still be detected at 1072, 970, 900, and 812 cm^{-1}, respectively. On the one hand, the existence of these characteristic bands indicates that the Keggin structure of the HPW is retained well in the composites upon undergoing high temperature hydrothermal reaction. On the other hand, the intensity of the characteristic peaks of HPW in the composites weakens, possibly due to the fewer HPW loadings. Simultaneously, the characteristic vibrational frequencies of HPW exhibit a shift compared with the parent HPW, implying that the occurrence of a strong interaction between the Keggin unit and $V_O^{\bullet}$–TiO_2 on the interface of the two components (Li et al. 2010a). The IR spectra result unravels that

the HPW not only was loaded onto the interface of $V_O^{\bullet}$–TiO_2 but also kept an intact Keggin structure.

The light absorption property of catalysts is one of main influence factors on photocatalytic activity. So, the UV–vis diffuse reflectance spectroscopy of the composites with the different HPW loadings and P25 used as reference sample as well as NTA served as TiO_2 precursor is tested. In Fig. 3a, compared with NTA(HCl)-150, namely $V_O^{\bullet}$–TiO_2, achieved by heat-treating NTA in acid medium, each HPW-loaded $V_O^{\bullet}$–TiO_2 sample shows a slight shift towards longer wavelength, and the shift gradually becomes obvious as increasing HPW loadings from 0.05 to 0.7 g relative to 1 g NTA. These observations are closely connected with the charge transfer from O 2p to the new conduction band formed by the hybridization of Ti 3d and W 5d orbit in view of the similar energy of them (Lu et al. 2012; Li et al. 2005). In Fig. 3b, the NTA and P25 only exhibit broad absorption bands in the UV region. Whereas, compared to P25 and NTA, NTA(HCl)-120 with a bandgap energy (E_g) of 2.84 eV (inset in Fig. 3b), obtained according to the same preparation process as the sample HPWN-0.1-120 only without the addition of HPW, shows an obvious redshift. The occurrence of the redshift is associated with the generated $V_O^{\bullet}$ during the heat treatment (Fig. 4), which would form an intermediate energy state close to the bottom of the conduction band within the bandgap of TiO_2, thus inducing the absorption in the visible light region (Zhang et al. 2004a, b; Wang et al. 2010, 2011; Li et al. 2015). In the case of as-fabricated composite material HPWN-0.1-120, only the slight shift towards long wavelength can be observed corresponding to the E_g value of 2.81 eV compared to NTA(HCl)-120. As has been noted, the mild redshift may be due to the charge transfer from O 2p to the new conduction band constructed by the hybridization of Ti 3d and W 5d orbits of the Keggin unit, indicating that the visible light absorption in hybrid photocatalysts mainly originated from the formed $V_O^{\bullet}$ during the heat treatment. In the work, the bandgap values of almost all photocatalysts have been calculated and listed in Table 1. As for $V_O^{\bullet}$ (single-electron-trapped oxygen vacancy), we tested its existence by electron spin resonance technique (ESR) that is a highly sensitive spectroscopic technique for examining paramagnetic species. As illustrated in Fig. 4, the samples HPWN-0.1-120 and HPWN-0.1-150 show ESR signal at $g = 2.004$ assigned to single-electron-trapped oxygen vacancy ($V_O^{\bullet}$) in consideration of the characteristic of NTA (Zhang et al. 2004a, b). As for the weaker ESR signal of HPWN-0.1-120 than that of HPWN-0.1-150 is due to that the high reaction temperature is more conducive to the generation of $V_O^{\bullet}$.

The morphologies, microstructures, and elemental distribution of the as-prepared samples were investigated using SEM, HRTEM, and EDS analyses, where we selected the composite HPWN-0.1-120 possessing the best photocatalytic activity (see photocatalysis section) as a representative sample to carry out characterization. As a comparison, the SEM and TEM images of the sample NTA(HCl)-120 were also given. Figure 5a shows that the morphology of the NTA(HCl)-120 and HPWN-0.1-120 consists of stacked and irregular particle-like structures, which is corresponding with the result from TEM (Fig. 6a, b). There is no obvious difference in morphologies for two catalysts. Moreover, from SEM and TEM images, we do not detect the

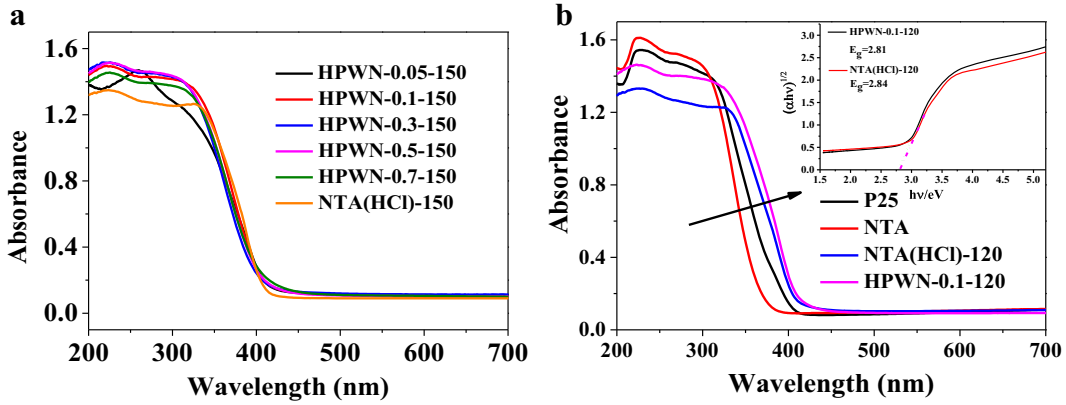

Fig. 3 UV–vis diffuse reflectance spectroscopy of P25, NTA, NTA(HCl)-120/150, and HPW/$V_O^{\bullet}$–TiO_2 composites with the different HPW loadings

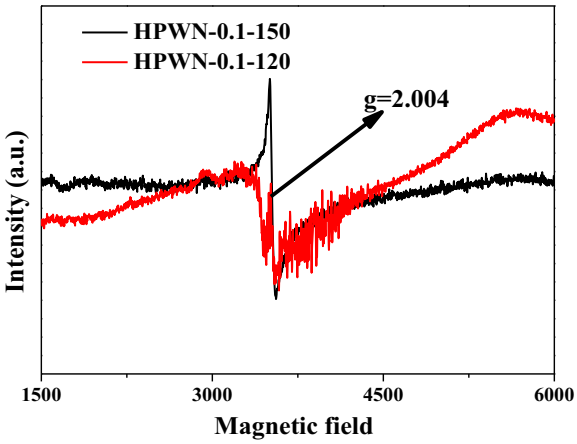

Fig. 4 ESR spectra of the composites HPWN-0.1-120 and HPWN-0.1-150

existence of HPW, probably due to the little loadings of HPW. And the size range of the achieved catalysts nanoparticles is about 10~50 nm according to TEM. In order to verify the presence of HPW and the formation of the composite between phosphotungstic acid and $V_O^{\bullet}$–TiO_2, SEM-EDS elemental mapping of the HPWN-0.1-120 sample was performed by operating the SEM in scanning mode. As revealed in Fig. 5c–f, we can clearly see that the Ti, O, P, and W elements were distributed homogeneously in the HPWN-0.1-120 composite, implying the coexistence of HPW and TiO_2 and the formation of the composite between HPW and TiO_2. Aforementioned, XRD pattern showed that the mixed phase of anatase and rutile coexisted in the HPWN-0.1-120. In order to give the further evidence, HRTEM analysis was conducted. In Fig. 6b, for HPWN-0.1-120, there are two kinds of lattice fringes observed with fringe spacing of ca. 0.35 nm consistent with the (101) plane of the anatase TiO_2 and that of 0.32 nm corresponding to the (110) lattice plane of the rutile TiO_2, suggesting the coexistence of two phases of anatase and rutile, consistent with the XRD result. The coexisted mixed phase is beneficial for separation of the photogenerated charge carriers, thus improving the photocatalytic activity (Yu et al. 2001, 2003; Xie et al. 2014).

Table 1 The estimated bandgap and initial rate of pollutant degradation (μmol/min) of the various photocatalysts

Photocatalysts	Bandgap (eV)	Initial rate (μmol/min)
HPWN-0.05-150	2.75	0.077
HPWN-0.1-150	2.79	0.137
HPWN-0.3-150	2.78	0.062
HPWN-0.5-150	2.74	0.087
HPWN-0.7-150	2.74	0.081
HPWN-0.1-120	2.81	0.228
HPWN-0.1-180	2.80	0.008
HPWN-0.1-200	2.76	0.035
NTA(HCl)-120	2.81	0.091
NTA(H_2O)-120	2.91	0.023
HPWN(H_2O)-0.1-120	2.83	0.159

Existing strong interactions between Keggin unit and $V_O^{\bullet}$–TiO_2 can be further confirmed by XPS spectra analysis. In the survey spectra shown in Fig. 7a, the survey spectrum of HPWN-0.1-120 reveals the existence of Ti, O, W, and P, demonstrating the formation of composite material of HPW and $V_O^{\bullet}$–TiO_2. As for the sample NTA(HCl)-120, the peaks at 458.3 and 464.1 eV of Ti 2p (Fig. 7b) corresponds to Ti $2p_{3/2}$ and Ti $2p_{1/2}$, respectively (Chen et al. 2016). However, after the addition of HPW, the peak values of Ti 2p provided by the sample HPWN-0.1-120 displays a shift towards the higher binding energy values, indicating the existence of the strong interactions on the interface of HPW and $V_O^{\bullet}$–TiO_2, which is due to the formation of the covalent W–O–Ti bonds through the interaction of the terminal W–O groups in the HPW Keggin units and the surface ≡Ti–OH groups of TiO_2 (Li et al. 2010a). This interaction is related to the loss of electrons on TiO_2 (Zhang et al. 2008; Rengifo-Herrera et al. 2016), namely the interaction resulted in the decreased electron density around Ti, thereby causing the binding energy shift to the higher energy value. In Fig. 7c, compared with the peaks of W 4f in pure HPW (36.1 and 38.2 eV for W $4f_{7/2}$ and W $4f_{5/2}$, respectively), an obvious decrease in the intensity of the W 4f peaks in HPWN-0.1-120 can be observed due to the little HPW loading (Rengifo-Herrera et al. 2016). Moreover, the binding energy values of W 4f in HPWN-0.1-120 show a shift towards the lower binding energy located at 35.7 eV (W $4f_{7/2}$) and 37.6 eV (W $4f_{5/2}$), which is contrary to the shift of Ti 2p peaks towards to high energy values, and but is consistent. The existence of interaction between the terminal W–O groups in the HPW Keggin units and the surface ≡Ti–OH groups of TiO_2 decreased electron density around Ti, concurrently, which increased electron density around W, thereby inducing the shift of binding energy of W 4f to lower value. For O 1s in HPWN-0.1-120, there are four peaks located at 529.9, 530.5, 531.9, and 533.3 eV, which is indexed into the lattice oxygen in

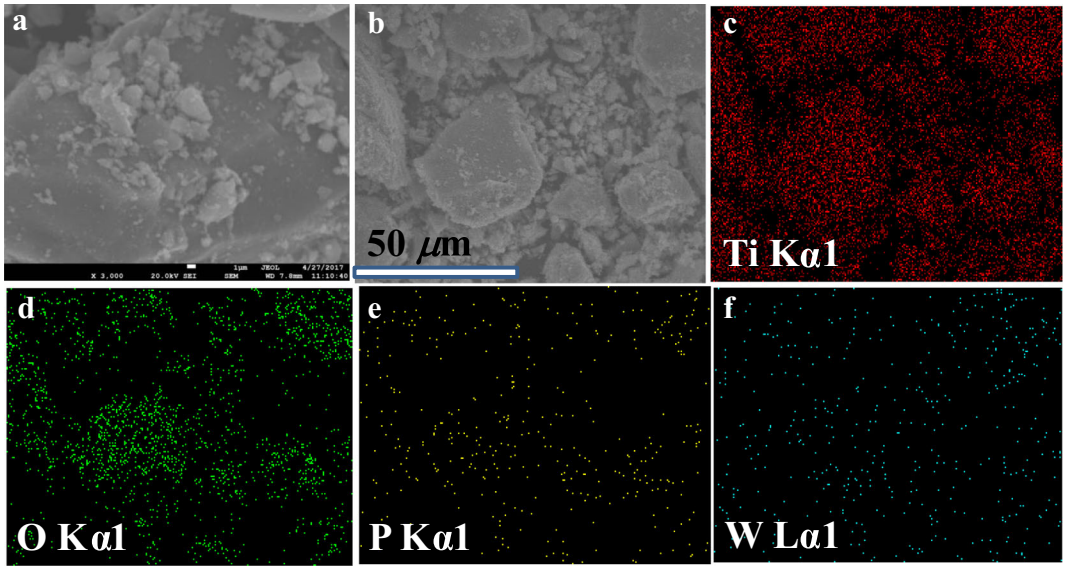

Fig. 5 FESEM image **a** NTA(HCl)-120, **b** HPWN-0.1-120, the element mapping images, **c** Ti, **d** O, **e** P, and **f** W in the HPWN-0.1-120

TiO_2, W–O–W, W–O–P/W–O–H in HPW and adsorbed water (Li et al. 2014), respectively (Fig. 7d).

Figure 8 displays N_2 adsorption–desorption isotherms along with the corresponding BJH pore size distribution plots of the samples NTA(H_2O)-120, NTA(HCl)-120, HPWN(H_2O)-0.1-120, and HPWN-0.1-120. The isotherms of all the samples show type IV adsorption isotherms along with a type I hysteresis loop, indicating the presence of mesoporosity, except for NTA(HCl)-120 (Storck et al. 1998). In Fig. 8a, b, comparing NTA(H_2O)-120 with NTA(HCl)-120, separately showing the anatase phase and rutile phase of TiO_2 (Fig. 1c), NTA(H_2O)-120 has a surface area of 138.27 m^2/g, but the surface area of NTA(HCl)-120 obtained in acid solvent decreased to 42.76 m^2/g. The decrease in surface area for NTA(HCl)-120 may be due to the formation of rutile. Rutile has a density of 4.23 g/cm^3 while anatase has a smaller density of 3.78 g/cm^3. The other reason is associated with the partial loss of mesoporosity (Luo et al. 2015). In inset of Fig. 8b, NTA(HCl)-120 has a wide pore size distribution from 3.41 to 29.65 nm and this sample displays a late adsorption edge ($p/p_0 > 0.9$) suggesting an increase in pore size. These observations accord with the decrease of BET surface area of NTA(HCl)-120. As for HPWN(H_2O)-0.1-120 and HPWN-0.1-120, prepared using water and hydrochloric acid as solvent separately, no significant difference in the surface area (185.81 m^2/g for HPWN(H_2O)-0.1-120 and 181.64 m^2/g for HPWN-0.1-120) was displayed, which may be due to the existence of the anatase as the main phase in HPWN-0.1-120 (Fig. 1c). This can be reflected from inset in Fig. 8c, d that BJH desorption pore size distributions are 5.54 nm for HPWN(H_2O)-0.1-120 and 3.82 nm for HPWN-0.1-120. Comparing NTA(HCl)-120 with HPWN-0.1-120, produced in hydrochloric acid solvent,

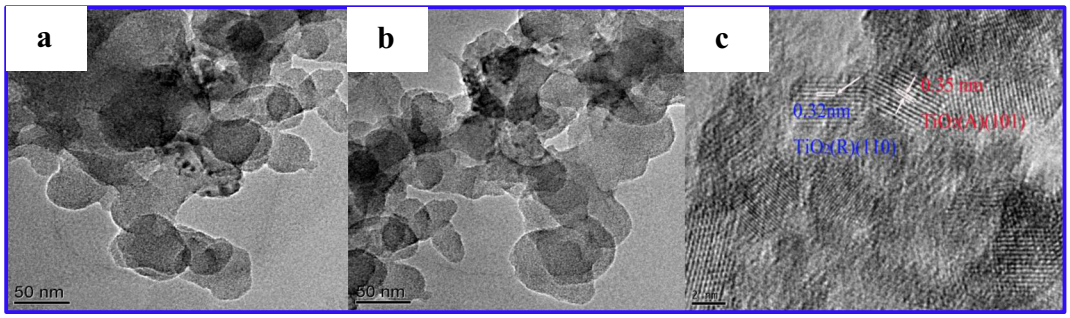

Fig. 6 TEM **a** NTA(HCl)-120, **b** HPWN-0.1-120, and **c** HRTEM images of HPWN-0.1-120

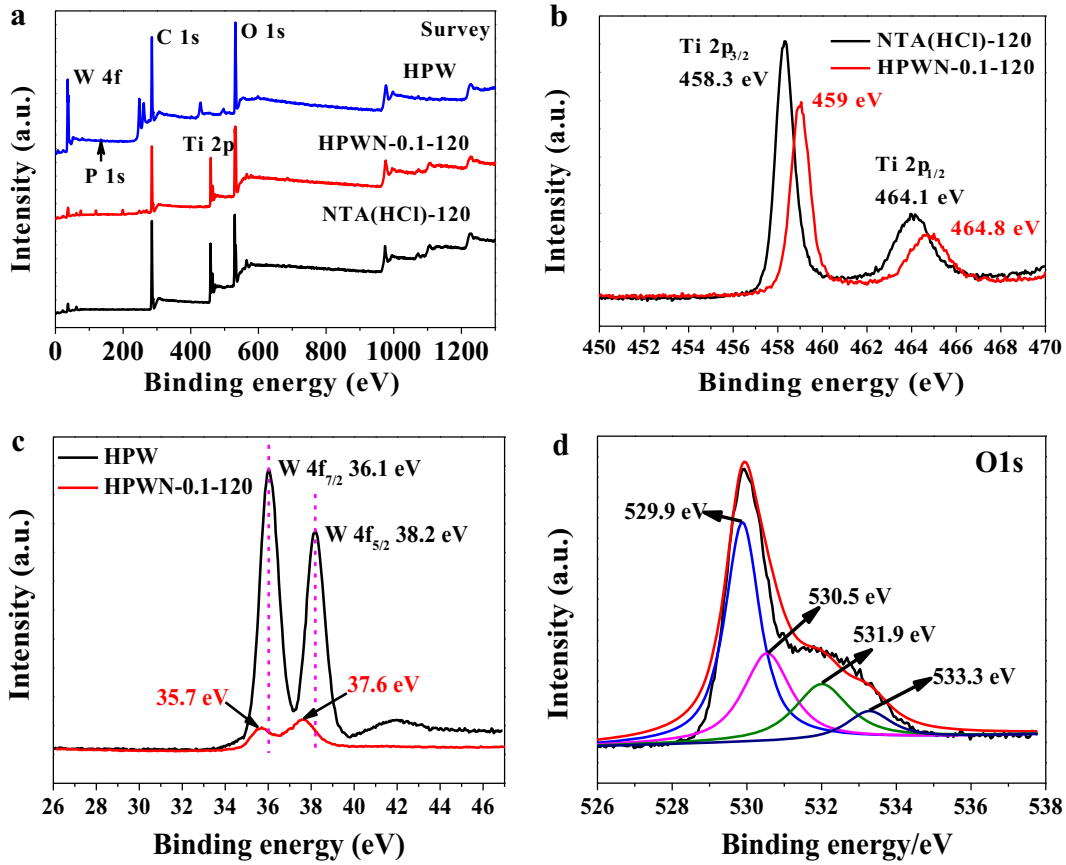

Fig. 7 XPS spectra of HPW, NTA(HCl)-120 and HPWN-0.1-120, **a** survey, **b** Ti 2p, **c** W 4f, and **d** O 1s

distinct difference of BET area and pore size distribution can be found, likewise owing to main phase of anatase. Meanwhile, this also means that HPW may restrain the growth of rutile corresponding to XRD.

In order to study the effect of the HPW loading on the photocatalytic activity of $V_O^{\bullet}$–TiO_2, 100 mL of RhB solution (20 mg/L) was used as model pollutant. The photodegradation experiments of catalysts were carried out under visible light irradiation ($\lambda > 420$ nm). Before irradiation, the suspension was kept in dark for 2 h to achieve the adsorption–desorption equilibrium between photocatalysts and reaction substrate. As displayed in Fig. 9a, in the selected range of the HPW loading (from 0.05 to 0.7 g), all the composites showed an obvious enhancement of photocatalytic efficiency for the photodegradation of RhB with visible light, indicating that the loading of HPW on $V_O^{\bullet}$–TiO_2 is advantageous to facilitate photocatalytic activity. At the same time, it can be found from Fig. 9a that the photoactivity strongly depended on the HPW loading content. The sample HPWN-0.1-150 obtained with a designed loading content of 0.1 g HPW and at 150 °C exhibited the highest photocatalytic efficiency, on which RhB was almost completely decomposed in the time of 40-min irradiation. The obtained composites at the different hydrothermal temperature always showed the different morphology, crystal structure as well as photo-absorption properties, which affects the photocatalytic activity of catalysts in turn. Considering this, a series of composites with 0.1 g HPW loading were fabricated under the different hydrothermal temperature (120, 180, and 200 °C). The as-prepared sample HPWN-0.1-120 exhibits the higher photodegradation rate that RhB is completely degraded after irradiation of 40 min (Fig. 9b, e). This can be explained as follows: the sample HPWN-0.1-120 shows the mixed phase of anatase and rutile (Fig. 1b), which would boost the separation efficiency of the photoinduced electron–hole pairs and thus enhancing photocatalytic activity. Figure 9c, d shows the photodegradation kinetics of RhB over the achieved photocatalysts. In the studied concentration and hydrothermal temperature range, the photocatalytic

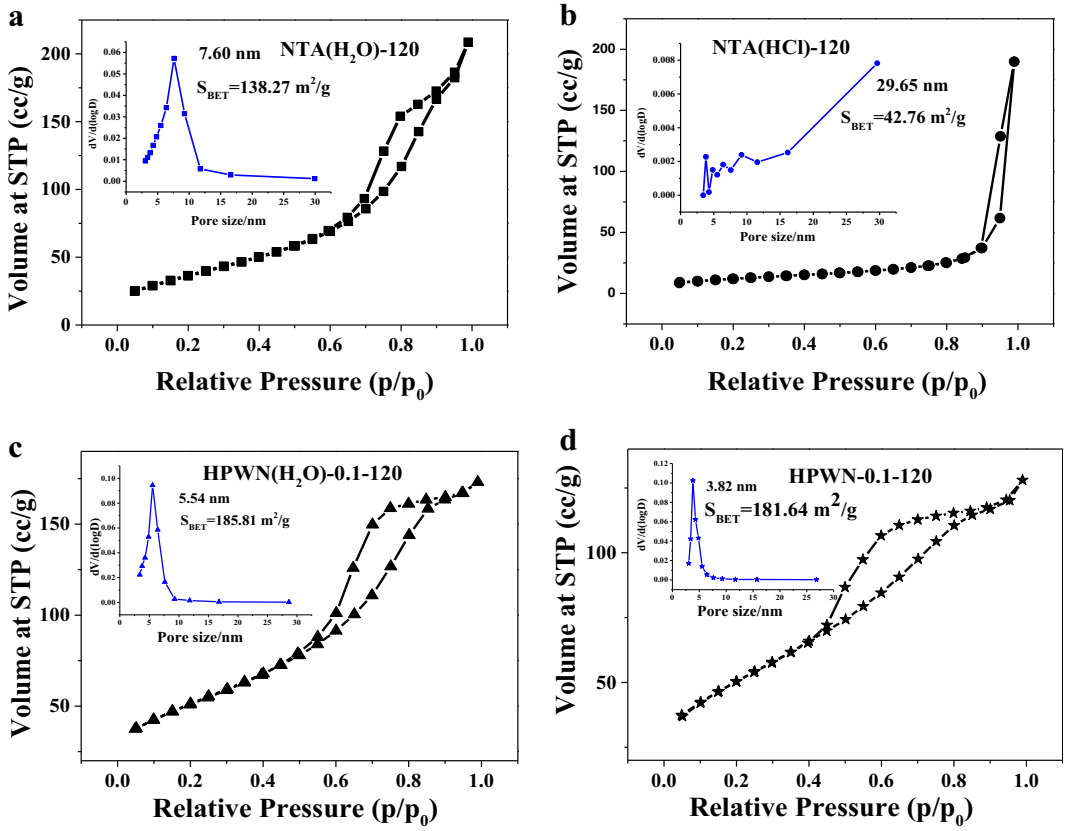

Fig. 8 N_2 adsorption–desorption isotherm of **a** NTA(H_2O)-120, **b** NTA(HCl)-120, **c** HPWN(H_2O)-0.1–120, and **d** HPWN-0.1-120. The insets are the corresponding BJH desorption pore-size distributions of each sample **a** 7.60, **b** 29.65, **c** 5.54, and **d** 3.82 nm

degradation appears to follow pseudo first-order reaction kinetics, and HPWN-0.1-120 gave the highest apparent rate constant with $k_{app} = 0.116\ min^{-1}$. In addition, taking HPWN-0.1-120 as a representative, the calculated apparent quantum efficiency was about 0.143%.

To further verify much higher photocatalytic activity displayed by the composite samples, we gave a comparative result of HPWN-0.1-120 with other catalysts in activity. As revealed in Fig. 9f, in the absence of catalyst, no obvious photodegradation of RhB is observed, meaning that no photosensitization exists for RhB. Without addition of HPW, we firstly compared the photo-decomposition activity of NTA(H_2O)-120 and NTA(HCl)-120 that were fabricated in pure water and acid medium, separately. Clearly, compared to NTA(H_2O)-120 showing single anatase phase, NTA(HCl)-120 with rutile phase displays the enhanced photodegradation rate for RhB, maybe due to the rutile TiO_2 possessing the narrower bandgap value (Fig. 9g) though the clear difference in BET area. After the addition of HPW, both HPWN-0.1-120 and HPWN(H_2O)-0.1-120, fabricated in acid and pure water medium respectively, show the dramatically enhanced photocatalytic performance, suggesting that the loading of phosphotungstic acid as an effective electron acceptor can improve forcefully segregation of charge carries. But comparatively, HPWN-0.1-120 gave activity exceeding HPWN(H_2O)-0.1-120, which is intimately connected with the formation of the mixed-phase structure (Fig. 1b) further decreasing the recombination rate of photoinduced electron–hole. Based on the abovementioned analysis, we can readily conclude that the co-effect of the anatase TiO_2, the rutile TiO_2

Fig. 9 Photocatalytic degradation curves of RhB **a** HPWN-*x*-150 (*x* = 0.05, 0.1, 0.3, 0.5, 0.7), **b** HPWN-0.1-T (*T* = 120, 150, 180, 200), photodegradation kinetic curves of RhB **c** HPWN-*x*-150 (*x* = 0.05, 0.1, 0.3, 0.5, 0.7), **d** HPWN-0.1-T (*T* = 120, 150, 180, 200). **e** The absorbance changes of RhB solution after irradiation on HPWN-0.1-120, the inset is the color changes. **f** Comparison of photocatalytic efficiency of RhB on various photocatalysts. **g** UV–vis adsorption spectra of NTA(HCl)-120 and NTA(H_2O)-120. **h** The effect of hydrochloric acid concentration on photocatalytic efficiency ▶

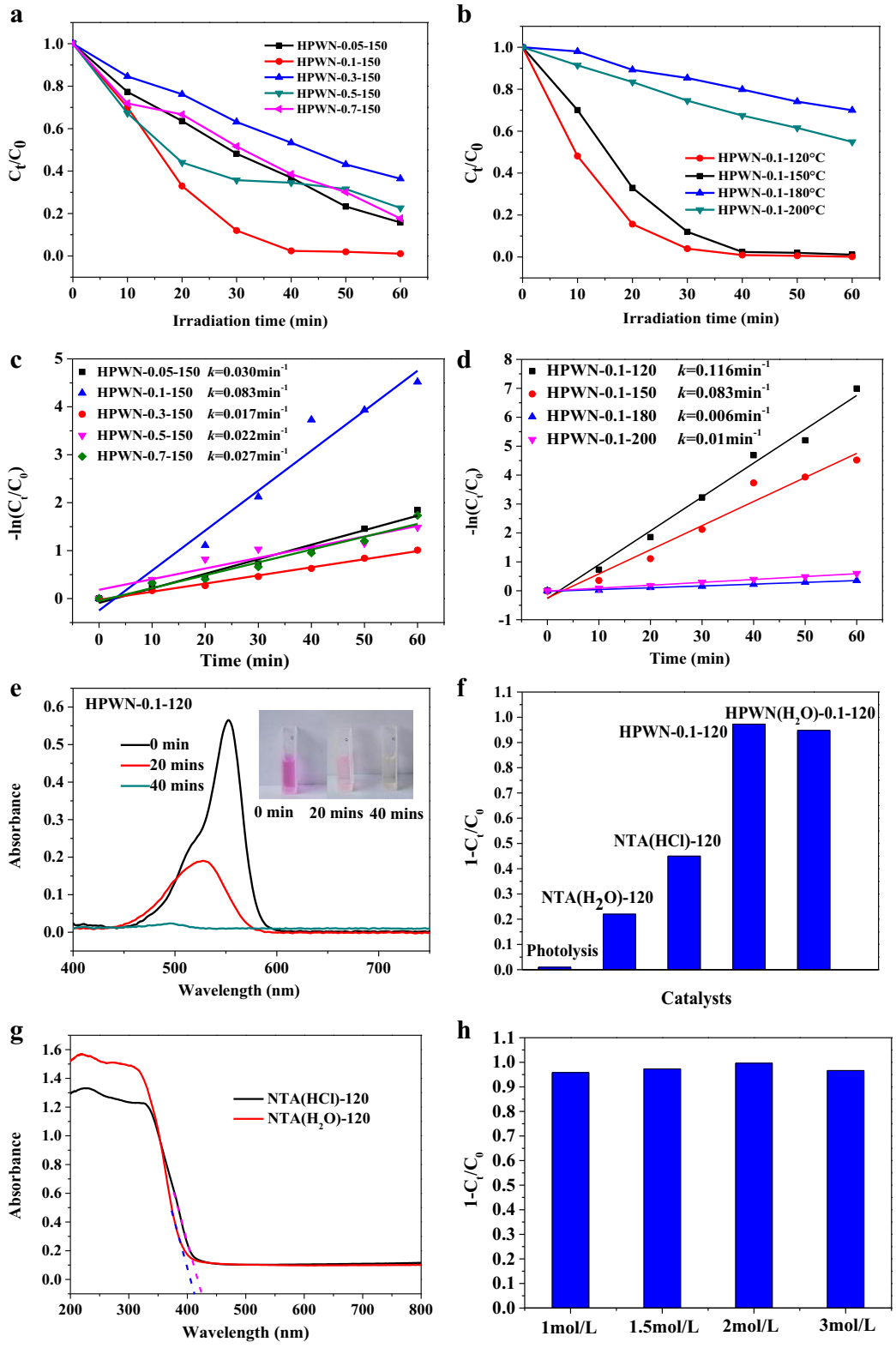
a
HPWN-0.05-150
HPWN-0.1-150
HPWN-0.3-150
HPWN-0.5-150
HPWN-0.7-150
C_t/C_0
Irradiation time (min)
b
HPWN-0.1-120°C
HPWN-0.1-150°C
HPWN-0.1-180°C
HPWN-0.1-200°C
C_t/C_0
Irradiation time (min)
c
HPWN-0.05-150 k=0.030min-1
HPWN-0.1-150 k=0.083min-1
HPWN-0.3-150 k=0.017min-1
HPWN-0.5-150 k=0.022min-1
HPWN-0.7-150 k=0.027min-1
$-\ln(C_t/C_0)$
Time (min)
d
HPWN-0.1-120 k=0.116min-1
HPWN-0.1-150 k=0.083min-1
HPWN-0.1-180 k=0.006min-1
HPWN-0.1-200 k=0.01min-1
$-\ln(C_t/C_0)$
Time (min)
e
HPWN-0.1-120
0 min
20 mins
40 mins
0 min 20 mins 40 mins
Absorbance
Wavelength (nm)
f
HPWN(H2O)-0.1-120
HPWN-0.1-120
NTA(HCl)-120
NTA(H2O)-120
Photolysis
$1-C_t/C_0$
Catalysts
g
NTA(HCl)-120
NTA(H2O)-120
Absorbance
Wavelength (nm)
h
$1-C_t/C_0$
1mol/L
1.5mol/L
2mol/L
3mol/L

and HPW leads to the greatly enhanced photoactivity of HPWN-0.1-120. In this system, the loading of HPW significantly enhanced the separation efficiency of photogenerated electron–hole pairs, while the presence of oxygen vacancy induced the photo-absorption of catalyst in visible light. Further, we studied the effect of hydrochloric acid concentration used during the catalysts preparation on photocatalytic activity. In Fig. 9h, it can be seen that the highest photoactivity was obtained upon 2 mol/L HCl as solvent.

As has been noted, the achieved higher visible light-targeted photocatalytic efficiency for the sample HPWN-0.1-120 should be attributed to the following three aspects: (a) oxygen vacancy, (b) the unique mixed phase of anatase and rutile mesoporous structure, and (c) the presence of HPW. As described in introduction, the generated $V_O^{\bullet}$ during the heat treatment formed a localized impurity level located at 0.9–1.2 eV below the conduction band of TiO_2 according to our theoretical calculation (Wang et al. 2011). The formed $V_O^{\bullet}$ can induce visible light absorption of catalyst, which is prerequisite arising visible light catalytic activity. Secondly, the formation of the unique mixed phase improves effectively charge carrier separation, thereby contributing to the enhanced photocatalytic activity, which was reported by many research groups (Li and Gray 2007; Lei and Duan 2008; Murakami et al. 2010; Yu et al. 2005, 2001, 2003). From Fig. 10, the rutile phase TiO_2 has a lower bandgap energy than anatase TiO_2 (3.03 vs 3.2 eV) (Hegazy and Prouzet 2012), and the CB and VB levels of anatase TiO_2 are positive to the corresponding levels of rutile TiO_2 (Scanlon et al. 2013). When these two phases combined, a staggered bandgap can be produced and cause a greatly enhanced the separation efficiency of the electron–hole pairs along phase junctions due to the formation of a type-II heterojunction between the anatase and the rutile. With visible light irradiation, the photogenerated electrons

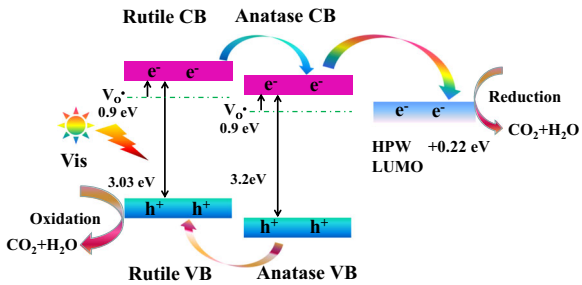

Fig. 10 Schematic diagram of photocatalytic mechanism

from rutile CB can migrate to anatase CB, thus retarding the recombination of the electron–hole pairs in rutile phase, which can be demonstrated by transient photocurrent response test in Fig. 11a. As expected, HPWN-0.1-120 composed of the mixed phase of anatase and rutile shows the much larger photocurrent response than that of HPWN(H_2O)-0.1-120 consisting of pure anatase phase (Fig. 1c), implying that HPWN-0.1-120 possesses the higher electron–hole separation rate. Clearly, this is closely related to the formation of the phase heterojunction between the anatase and rutile. Figure 11b gave the EIS Nyquist plots of HPWN-0.1-120 and HPWN(H_2O)-0.1-120. It can be found that the arc radius on EIS Nyquist plot of HPWN-0.1-120 is smaller than that of HPWN(H_2O)-0.1-120, meaning that a fast interfacial charge-transfer process and effective separation of photogenerated electron–hole pairs, according to the results from photocurrent response.

HPW loading further allowed the enhancement of the separation rate of the electron–hole pairs owing to the formation of surface heterojunctions between anatase and HPW. As mentioned in introduction, 12-tungstophosphoric acid ($H_3PW_{12}O_{40}$) with a well-defined Keggin structure can be viewed as an efficient electron trap because photogenerated electrons are trapped in the unoccupied W 5d states of the Keggin unit, which has already been proved by many researchers (Li et al. 2010a, b; Xu et al. 2010; Lu et al. 2012; Zhang et al. 2012). The LUMO level of HPW is about + 0.22 eV (Sun et al. 2015), be positive than that of conduction band of anatase, indicating that the photogenerated electrons accumulated at anatase CB could transfer from the anatase CB to HPW to further reduce the electron–hole recombination rate. Concurrently, the holes would accumulate at the negative valence band of rutile. Followingly, both the electrons in LUMO energy of HPW and the holes in VB of rutile participate in photocatalytic reaction to decompose organic contaminant RhB. Of course, the higher surface areas of HPW/$V_O^{\bullet}$–TiO_2 composite materials were also beneficial to enhancing their photocatalytic activity. To give a further evidence of HPW as an effective electron acceptor, we synthetized the catalyst HPWP25-0.1-120 with commercial P25 TiO_2 as starting material composed of the mixed phase of rutile and anatase and tested fluorescence spectrum of it and P25. In Fig. 11c, the PL intensity of HPWP25-0.1-120 obviously weakened, meaning that the presence of HPW can effectively inhibit the annihilation of the photogenerated electron–

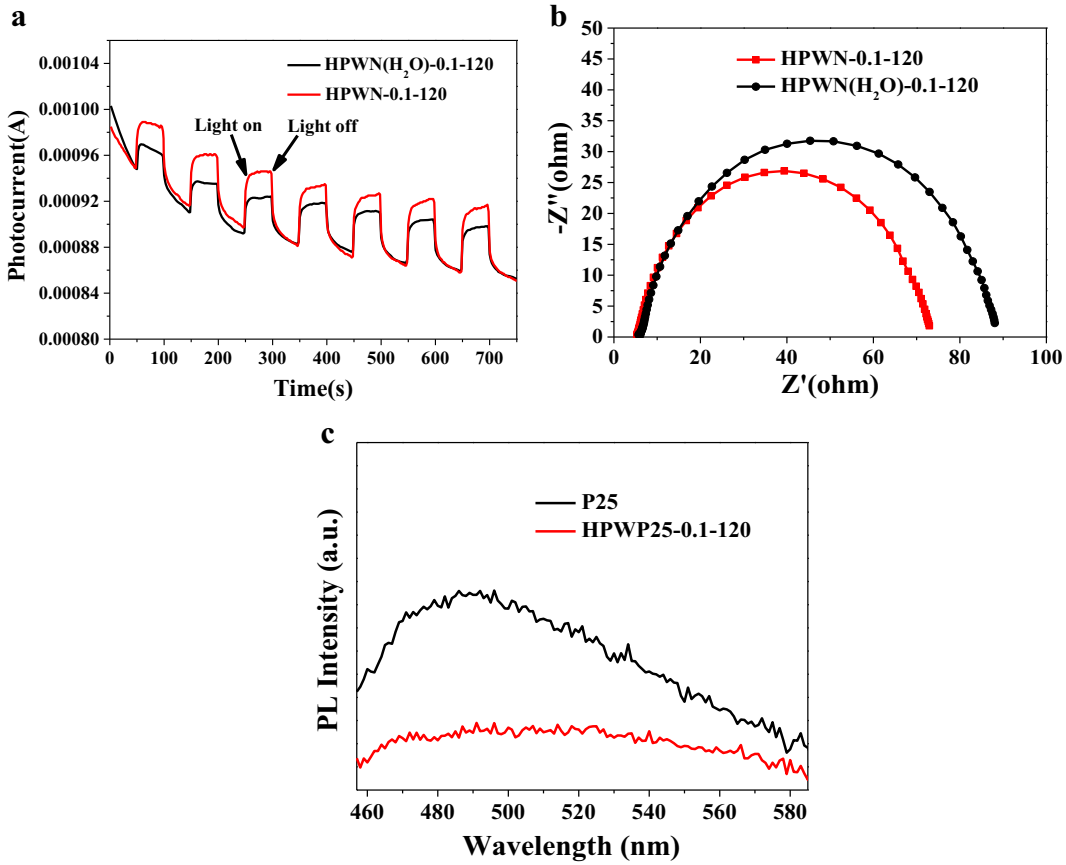

Fig. 11 **a** Transient photocurrent response. **b** Electrochemical impedance spectroscopy. **c** PL spectra

hole pairs. Just because of the synergistic effect of phase heterojunction of rutile/anatase, surface heterojunction of anatase/HPW, and $V_O^{\bullet}$, HPWN-0.1-120 achieved the gratifying visible light-driven photocatalytic efficiency.

Conclusions

We have explored effective photocatalysts in a simple hydrothermal process by loading HPW onto TiO_2 modified by $V_O^{\bullet}$ in acid medium. Significantly, the produced complex photocatalysts promote greatly the decomposition of RhB (20 mg/L), which is completely degraded in 40 min of visible light. The co-effect of phase heterojunction of rutile/anatase, surface heterojunction of anatase/HPW, and oxygen vacancy ($V_O^{\bullet}$) contributed to the efficient decomposition of RhB under visible light irradiation, in which these two-type heterojunction promoted greatly the photogenerated charge carrier separation efficiency and oxygen vacancy lured absorption of catalysts in the visible light region. In this case, the photoelectrons on the CB of rutile could transfer to the CB of anatase and then moved LUMO of HPW to decrease enormously the recombination rate, whereas the photoholes transfer from the VB of anatase to the VB of rutile to carry out oxidizing reaction for the degradation of RhB.

Funding This work has been supported by the National Natural Science Foundation of China (21471045, 21571049), the Natural Science Foundation of Henan Province of China (162300410027, 162300410013), the Foundation of the Education Department of Henan Province of China (13A150045), Open Research Funds of Henan Key Laboratory of Polyoxometalate Chemistry (HNPOMKF1607, HNPOMKF1701), and the Scientific Fund of Henan Province Postdoctor (in 2016, First Aid).

Compliance with ethical standards

Conflict of interest The authors declare that they have no conflict of interest.

References

Asahi R, Morikawa T, Ohwaki T, Aoki K, Taga Y (2001) Visible-light photocatalysis in nitrogen-doped titanium oxides. Science 293(5528):269–271. https://doi.org/10.1126/science.1061051

Chen W, Liu TY, Huang T, Liu XH, Duan GR, Yang XJ, Chen SM (2015) Novel yet simple strategy to fabricate visible light responsive C,N-TiO_2/g-C_3N_4 heterostructures with significantly enhanced photocatalytic hydrogen generation. RSC Adv 5(122):101214–101220. https://doi.org/10.1039/C5RA18302B

Chen Y, Li WZ, Wang JY, Gan YL, Liu L, Ju MT (2016) Microwave-assisted ionic liquid synthesis of Ti^{3+} self-doped TiO_2 hollow nanocrystals with enhanced visible-light photoactivity. Appl Catal B 191:94–105. https://doi.org/10.1016/j.apcatb.2016.03.021

Choi W, Termin A, Hoffmann MR (1994) The role of metal ion dopants in quantum-sized TiO_2: correlation between photoreactivity and charge carrier recombination dynamics. J Phys Chem 98(51):13669–13679. https://doi.org/10.1021/j100102a038

Dong GH, Ho WK, Zhang LZ (2015) Photocatalytic NO removal on BiOI surface: the change from nonselective oxidation to selective oxidation. Appl Catal B 168–169:490–496. https://doi.org/10.1016/j.apcatb.2015.01.014

Fujishima A, Honda K (1972) Electrochemical photolysis of water at a semiconductor electrode. Nature 238(79):37–38

Hegazy A, Prouzet E (2012) Room temperature synthesis and thermal evolution of porous nanocrystalline TiO_2 anatase. Chem Mater 24(2):245–254

Heng HM, Gan Q, Meng PC, Liu X (2017) The visible-light-driven typeIII heterojunction $H_3PW_{12}O_{40}$/TiO_2-In_2S_3: a photocatalysis composite with enhanced photocatalytic activity. J Alloy Compd 696:51–59. https://doi.org/10.1016/j.jallcom.2016.11.116

Hong YZ, Jiang YH, Li CS, Fan WQ, Yan X, Yan M, Shi WD (2016) In-situ synthesis of direct solid-state Z-scheme V_2O_5/g-C_3N_4, heterojunctions with enhanced visible light efficiency in photocatalytic degradation of pollutants. Appl Catal B 180:663–673. https://doi.org/10.1016/j.apcatb.2015.06.057

Karkas MD, Verho O, Johnston EV, Åkermark B (2014) Artificial photosynthesis: molecular systems for catalytic water oxidation. Chem Rev 114(24):11863–12001

Kasuga T, Hiramatsu M, Hoson A, Sekino T, Niihara K (1998) Formation of titanium oxide nanotube. Langmuir 14(12):3160–3163

Lei S, Duan W (2008) Highly active mixed-phase TiO_2 photocatalysts fabricated at low temperature and the correlation between phase composition and photocatalytic activity. J Environ Sci 20(10):1263–1267. https://doi.org/10.1016/S1001-0742(08)62219-6

Li GH, Gray KA (2007) Preparation of mixed-phase titanium dioxide nanocomposites via solvothermal processing. Chem Mater 19(5):1143–1146

Li L, Wu QY, Guo YH, Hu CW (2005) Nanosize and bimodal porous polyoxotungstate-anatase TiO_2 composites: preparation and photocatalytic degradation of organophosphorus pesticide using visible-light excitation. Micropor Mesopor Mater 87(1):1–9. https://doi.org/10.1016/j.micromeso.2005.07.035

Li KX, Guo YN, Ma FY, Li HC, Chen L, Guo YH (2010a) Design of ordered mesoporous $H_3PW_{12}O_{40}$-titania materials and their photocatalytic activity to dye methyl orange degradation. Catal Commun 11(9):839–843. https://doi.org/10.1016/j.catcom.2010.03.004

Li KX, Yang X, Guo YN, Ma FY, Li HC, Chen L, Guo YH (2010b) Design of mesostructured $H_3PW_{12}O_{40}$-titania materials with controllable structural orderings and pore geometries and their simulated sunlight photocatalytic activity towards diethyl phthalate degradation. Appl Catal B 99:364–375. https://doi.org/10.1016/j.apcatb.2010.07.012

Li KX, Yan LS, Zeng ZX, Luo SL, Luo XB, Liu XM, Guo HQ, Guo YH (2014) Fabrication of $H_3PW_{12}O_{40}$-doped carbon nitride nanotubes by one-step hydrothermal treatment strategy and their efficient visible-light photocatalytic activity toward representative aqueous persistent organic pollutants degradation. Appl Catal B 156–157:141–152. https://doi.org/10.1016/j.apcatb.2014.03.010

Li HY, Ren FZ, Liu JF, Wang QL, Li QY, Yang JJ, Wang YX (2015) Endowing single-electron-trapped oxygen vacancy self-modified titanium dioxide with visible-light photocatalytic activity by grafting Fe(III) nanocluster. Appl Catal B 172:37–45. https://doi.org/10.1016/j.apcatb.2015.02.008

Li X, Yu JG, Jaroniec M (2016) Hierarchical photocatalysts. Chem Soc Rev 45(9):2603–2636

Low JX, Cheng B, Yu JG (2017) Surface modification and enhanced photocatalytic CO_2 reduction performance of TiO_2. Appl Surf Sci 392:658–686. https://doi.org/10.1016/j.apsusc.2016.09.093

Lu N, Zhao YH, Liu HB, Guo YH, Yuan X, Xu H, Peng HF, Qin HW (2012) Design of polyoxometallate–titania composite film ($H_3PW_{12}O_{40}$/TiO_2) for the degradation of an aqueous dye rhodamine B under the simulated sunlight irradiation. J Hazard Mater 199–200:1–8. https://doi.org/10.1016/j.jhazmat.2011.08.070

Luo Z, Poyraz AS, Kuo CH, Miao R, Meng YT, Chen SY, Jiang T, Wenos C, Suib SL (2015) Crystalline mixed phase (anatase/rutile) mesoporous titanium dioxides for visible light photocatalytic activity. Chem Mater 27(1):6–17. https://doi.org/10.1021/cm5035112

Mattos de FCG, Carvalho de ENCB, Freitas de EF, Paiva MF, Ghesti GF, Macedo de JL, Dias SCL, Dias JA (2017) Acidity and characterization of 12-tungstophosphoric acid supported on silica-alumina. J Braz Chem Soc 28(2):336–347. https://doi.org/10.5935/0103-5053.20160183

Murakami N, Kamai T, Tsubota T, Ohno T (2010) Control of the crystal structure of titanium (IV) oxide by hydrothermal treatment of a titanate nanotube under acidic conditions. CrystEngComm 12(2):532–537

Prier CK, Rankic DA, MacMillan DWC (2013) Visible light photoredox catalysis with transition metal complexes: applications in organic synthesis. Chem Rev 113(7):5322–5363

Qu YQ, Duan XF (2013) Progress, challenge and perspective of heterogeneous photocatalysts. Chem Soc Rev 42(7):2568–2580

Rengifo-Herrera JA, Blanco M, Wist J, Florian P, Pizzio LR (2016) TiO_2 modified with polyoxotungstates should induce visible-light absorption and high photocatalytic activity

through the formation of surface complexes. Appl Catal B 189:99–109. https://doi.org/10.1016/j.apcatb.2016.02.033

Reza Gholipour M, Dinh CT, Beland F, Do TO (2015) Nanocomposite heterojunctions as sunlight-driven photocatalysts for hydrogen production from water splitting. Nanoscale 7(18):8187–8208. https://doi.org/10.1039/C4NR07224C

Ruales-Lonfat C, Barona JF, Sienkiewicz A, Bensimon M, Velez-Colmenares J, Benítez N, Pulgarín C (2015) Iron oxides semiconductors are efficient for solar water disinfection: a comparison with photo-Fenton processes at neutral pH. Appl Catal B 166−167:497–508. https://doi.org/10.1016/j.apcatb.2014.12.007

Scanlon DO, Dunnill CW, Buckeridge J, Shevlin SA, Logsdail AJ, Woodley SM, Catlow CRA, Powell MJ, Palgrave RG, Parkin IP, Watson GW, Keal TW, Sherwood P, Walsh A, Sokol AA (2013) Band alignment of rutile and anatase TiO_2. Nat Mater 12(9):798–801. https://doi.org/10.1038/nmat3697

Storck S, Bretinger H, Maier WF (1998) Characterization of micro- and mesoporous solids by physisorption methods and pore-size analysis. Appl Catal A 174(1–2):137–146. https://doi.org/10.1016/S0926-860X(98)00164-1

Sun ZX, Zhang YZ, Li N, Xu L, Wang TQ (2015) Enhanced photoconductivity of a polyoxometalate-TiO_2 composite for gas sensing applications. J Mater Chem C 3(24):6153–6157. https://doi.org/10.1039/C5TC00904A

Wang Y, Feng CX, Zhang M, Yang JJ, Zhang ZJ (2010) Enhanced visible light photocatalytic activity of N-doped TiO_2 in relation to single-electron-trapped oxygen vacancy and doped-nitrogen. Appl Catal B 100:84–90. https://doi.org/10.1016/j.apcatb.2010.07.015

Wang Y, Feng CX, Zhang M, Yang JJ, Zhang ZJ (2011) Visible light active N-doped TiO_2 prepared from different precursors: origin of the visible light absorption and photoactivity. Appl Catal B 104:268–274. https://doi.org/10.1016/j.apcatb.2011.03.020

Wang H, Lang XF, Hao R, Guo L, Li JH, Wang LH, Han XD (2016) Facet-defined AgCl nanocrystals with surface-electronic-structure-dominated photoreactivities. Nano Energy 19:8–16. https://doi.org/10.1016/j.nanoen.2015.11.022

White JL, Baruch MF, Pander JE III, Hu Y, Fortmeyer IC, Park JE, Zhang T, Liao K, Gu J, Yan Y, Shaw TW, Abelev E, Bocarsly AB (2015) Light-driven heterogeneous reduction of carbon dioxide: photocatalysts and photoelectrodes. Chem Rev 115(23):12888–12935. https://doi.org/10.1021/acs.chemrev.5b00370

Willkomm J, Orchard KL, Reynal A, Pastor E, Durrant JR, Reisner E (2016) Dye-sensitised semiconductors modified with molecular catalysts for light-driven H_2 production. Chem Soc Rev 45(1):9–23. https://doi.org/10.1039/C5CS00733J

Wu MM, Lin G, Chen DH, Wang GG, He D, Feng SH, Xu RR (2002) Sol-hydrothermal synthesis and hydrothermally structural evolution of nanocrystal titanium dioxide. Chem Mater 14(5):1974–1980. https://doi.org/10.1021/cm0102739

Xie YJ, Wu ZJ, Zhang X, Ma PJ, Piao LY (2014) Nuclear factor-Kb-a pivotal transcription factor in chronic inflammatory diseases. Progress Chemistry 26(7):1120–1131. https://doi.org/10.7536/PC140124

Xu L, Yang X, Guo YH, Ma FY, Guo YN, Yuan X, Huo MX (2010) Simulated sunlight photodegradation of aqueous phthalate esters catalyzed by the polyoxotungstate/titania nanocomposite. J Hazard Mater 178(1–3):1070–1077. https://doi.org/10.1016/j.jhazmat.2010.02.049

Xu HQ, Hu JH, Wang DK, Li ZH, Zhang Q, Luo Y, Yu SH, Jiang HL (2015) Visible-light photoreduction of CO_2 in a metal–organic framework: boosting electron–hole separation via electron trap states. J Am Chem Soc 137(42):13440–13443. https://doi.org/10.1021/jacs.5b08773

Yang JJ, Jin ZS, Wang XD, Li W, Zhang JW, Zhang SL, Guo XY, Zhang ZJ (2003) Study on composition, structure and formation process of nanotube $Na_2Ti_2O_4(OH)_2$. Dalton Trans (20):3898–3901. https://doi.org/10.1039/B305585J

Yin S, Uchida S, Fujishiro Y, Aki M, Sato T (1999) Phase transformation of protonic layered tetratitanate under solvothermal conditions. J Mater Chem 9(5):1191–1195. https://doi.org/10.1039/A808064J

Yu JC, Yu JG, Ho WK, Zhang LZ (2001) Preparation of highly photocatalytic active nano-sized TiO_2 particles via ultrasonic irradiation. Chem Commun (19):1942–1943. https://doi.org/10.1039/B105471F

Yu JG, Yu JC, Leung MKP, Ho WK, Cheng B, Zhao XJ, Zhao JC (2003) Effects of acidic and basic hydrolysis catalysts on the photocatalytic activity and microstructures of bimodal mesoporous titania. J Catal 217(1):69–78. https://doi.org/10.1016/S0021-9517(03)00034-4

Yu JG, Xiong JF, Cheng B, Liu SW (2005) Fabrication and characterization of Ag-TiO_2, multiphase nanocomposite thin films with enhanced photocatalytic activity. Appl Catal B 60:211–221. https://doi.org/10.1016/j.apcatb.2005.03.009

Yu JG, Low JX, Xiao W, Zhou P, Jaroniec M (2014) Enhanced photocatalytic CO_2-reduction activity of anatase TiO_2 by coexposed {001} and {101} facets. J Am Chem Soc 136(25):8839–8842. https://doi.org/10.1021/ja5044787

Zhang M, Jin ZS, Zhang JW, Guo XY, Yang JJ, Li W, Wang XD, Zhang ZJ (2004a) Effect of annealing temperature on morphology, structure and photocatalytic behavior of nanotubed $H_2Ti_2O_4(OH)_2$. J Mol Catal A 217(1–2):203–210. https://doi.org/10.1016/j.molcata.2004.03.032

Zhang SL, Li W, Jin ZS, Yang JJ, Zhang JW, Du ZL, Zhang ZJ (2004b) Study on ESR and inter-related properties of vacuum-dehydrated nanotubed titanic acid. J Solid State Chem 177(4–5):1365–1371. https://doi.org/10.1016/j.jssc.2003.11.027

Zhang H, Wang G, Chen D, Lv XJ, Li JH (2008) Tuning photoelectrochemical performances of Ag-TiO_2 nanocomposites via reduction/oxidation of Ag. Chem Mater 20(20):6543–6549. https://doi.org/10.1021/cm801796q

Zhang SQ, Chen L, Liu HB, Guo W, Yang YX, Guo YH, Huo MX (2012) Design of $H_3PW_{12}O_{40}/TiO_2$ and Ag/$H_3PW_{12}O_{40}/TiO_2$ film-coated optical fiber photoreactor for the degradation of aqueous rhodamine B and 4-nitrophenol under simulated sunlight irradiation. Chem Eng J 200–202:300–309. https://doi.org/10.1016/j.cej.2012.06.060

Zhang JY, Wang YH, Jin J, Zhang J, Lin Z, Huang F, Yu JG (2013) Efficient visible-light photocatalytic hydrogen evolution and enhanced photostability of core/shell CdS/g-C_3N_4

nanowires. ACS Appl Mater Interfaces 5(20):10317–10324. https://doi.org/10.1021/am403327g

Zhang L, Wang WZ, Jiang D, Gao ER, Sun SM (2015) Photoreduction of CO_2 on BiOCl nanoplates with the assistance of photoinduced oxygen vacancies. Nano Res 8(3): 821–831. https://doi.org/10.1007/s12274-014-0564-2

Zhu SY, Liang SJ, Gu Q, Xie LY, Wang JX, Ding ZX, Liu P (2012) Effect of Au supported TiO_2 with dominant exposed {001} facets on the visible-light photocatalytic activity. Appl Catal B 119−120:146–155. https://doi.org/10.1016/j.apcatb.2012.02.020